CRYSTAL GROWTH & DESIGN



Article

# Experimental, Structural, and Computational Investigation of Mixed Metal-Organic Frameworks from Regioisomeric Ligands for Porosity Control

Dopil Kim, Hyeonbin Ha, Youngik Kim, Younghu Son, Jiyoon Choi, Myung Hwan Park, Youngjo Kim, Minyoung Yoon, Hyungjun Kim, Dongwook Kim, and Min Kim

*Cryst. Growth Des.*, **Just Accepted Manuscript** • DOI: 10.1021/acs.cgd.0c00562 • Publication Date (Web): 23 Jun 2020

# Experimental, Structural, and Computational Investigation of Mixed Metal-Organic Frameworks from Regioisomeric Ligands for Porosity Control

*Dopil Kim,[†,#] Hyeonbin Ha,[†,#] Youngik Kim,[†] Younghu Son,[‡] Jiyoon Choi,[§,∥] Myung Hwan Park,[¶]*

*Youngjo Kim,[†] Minyoung Yoon,*[‡] Hyungjun Kim,*[§,∥] Dongwook Kim,*[⊿] and Min Kim*[†]*

[†]Department of Chemistry, Chungbuk National University, Cheongju, 28644, Republic of Korea

[‡]Department of Chemistry, Kyungpook National University, Daegu, 41566, Republic of Korea

[§]Department of Chemistry, Incheon National University, Incheon, 22012, Republic of Korea

[∥]Research Institute of Basic Sciences, Incheon National University, Incheon, 22012, Republic of Korea

[¶]Department of Chemistry Education, Chungbuk National University, Cheongju, 28644, Republic of Korea

[Δ]Center for Catalytic Hydrocarbon Functionalization, Institute for Basic Science (IBS), Daejeon, 34141, Republic of Korea

KEYWORDS: metal-organic frameworks; regioisomer; functional groups; porosity; dimethoxy

ABSTRACT: Porosity control and structural analysis of metal-organic frameworks (MOFs) can be achieved using regioisomeric ligand mixtures. While *ortho*-dimethoxy-functionalized MOFs yielded highly porous structures and *para*-dimethoxy-functionalized MOFs displayed almost non-porous properties in their $N_2$ isotherms after evacuation, regioisomeric ligand-mixed MOFs showed variable $N_2$ uptake amount and surface area depending on the ligand-mixing ratio. The quantity of $N_2$ absorbed was tuned between 20 and 300 $cm^3/g$ by adjusting the ligand-mixing ratio. Both experimental analysis and computational modeling were performed to understand the porosity differences between *ortho*- and *para*-dimethoxy-functionalized MOFs. Detailed structural analysis using X-ray crystallographic data revealed significant differences in the coordination environments of DMOF-[2,3-$(OMe)_2$] and DMOF-[2,5-$(OMe)_2$] (DMOF = dabco MOF, dabco = 1,4-diazabicyclo[2.2.0]octane). The coordination bond between $Zn^{2+}$ and carboxylate in the *ortho*-functionalized DMOF-[2,3-$(OMe)_2$] was more rigid than that in the *para*-functionalized DMOF-[2,5-$(OMe)_2$]. Quantum chemical simulation also showed differences in the coordination environments of Zn-SBU (secondary building unit) surrounded by methoxy-functionalized ligands and pillar ligands. In addition, the binding energy differences between $Zn^{2+}$ and regioisomeric ligands (*ortho*- and *para*-dimethoxy-functionalized BDCs, BDC = benzene-1,4-

dicarboxylate) explained the rigidity and porosity changes of the mixed MOFs upon evacuation, and perfectly matched with experimental $N_2$ adsorption and X-ray crystallography data.

## INTRODUCTION

Metal-organic frameworks (MOFs) are emerging porous materials composed of infinitely repeating coordination bonds between metal clusters (or ions) and multivalent ligands. Although MOFs are generally synthesized under solvothermal conditions, empty pores can be generated by solvent evacuation under vacuum. The permanent porosity of MOFs, which has been utilized in various fields such as gas separation and molecular storage, has been intensively studied over the past two decades.[1–5] Because MOFs can be tuned at their metal cluster or ligands, porosity changes have been investigated in non-porous and highly porous materials as a function of structural changes. Isoreticular synthesis allows for the preparation of a series of MOFs with the same (or similar) topology but different porosities.[6]

Functionalization is also a key strategy for achieving porosity changes. When a bulky substituent is introduced at the ligand portion of the MOFs, decreased porosity is generally observed. For example, bromo-functionalized and naphthyl-functionalized zirconium-based UiO-66 (UiO-O = University of Oslo) showed a much lower porosity than pristine, non-functionalized UiO-66.[7] Although the functionalization method provides a series of MOFs with the same framework but different porosities, the extent of the change is not directly predictable. In addition, the synthesis and properties of MOFs can be altered by additional functionality on the ligand.[8]

The third approach for the porosity control of MOFs is structural flexibility. The MOF framework can be flexible under some conditions, such as in pillared MOFs, and the structure of

MOFs and porosity can also be changed upon application of external stimuli.[9,10] Gas pressure is a common stimuli for MOF flexibility control. Therefore, porosity control of flexible MOFs under standard conditions (*e.g.*, 1 atm) remains quite difficult. Recently, the correlation between functional group regioisomerism and MOF structural flexibility has been revealed using various combinations of chemical tags within pillared DMOFs (DMOF = dabco MOFs; DABCO = 1,4-diazabicyclo[2.2.0]octane).[11–13] DMOF contains a dimeric paddle-wheel-type SBU (secondary building unit) as a MOF node[14] and can exhibit structural flexibility. Recently, the flexibility of DMOFs was altered by the position of the functional group (*i.e.*, regioisomerism).[11] From comparison experiments with various functional group combinations, the electron density of the MOF ligand was shown to be correlated with the flexibility of DMOFs by Hammett plots.[12,13] Electron-rich combinations such as $NH_2$-OMe, $NH_2$-X, and OMe-OMe at the *para*-positions yielded flexible DMOFs upon evacuation, while *ortho*-$NH_2$-OMe, $NH_2$-X, and OMe-OMe along with other electron-deficient combinations resulted in an inflexible framework. In other words, although both DMOF-[2,3-$(OMe)_2$] and DMOF-[2,5-$(OMe)_2$] contain identical frameworks from solvothermal synthesis (*i.e.*, as-synthesized status), as indicated by powder X-ray diffraction patterns (PXRD), the porosities of the two DMOFs differ after evacuation. While *ortho*-functionalized, electron-rich, DMOF-[2,3-$(OMe)_2$] showed a pore volume of 0.329 $cm^3/g$ after evacuation (inflexible framework to evacuation), *para*-functionalized DMOF-[2,5-$(OMe)_2$] displayed an almost non-porous value of 0.085 $cm^3/g$ after evacuation (flexible framework to evacuation).[13] Although these extreme differences between the *ortho*- and *para*-regioisomers within electron-rich ligands are unique and interesting, the fine-control of MOF flexibility to evacuation remains a difficult task.

Herein, a mixed ligand strategy between *para*-dimethoxy and *ortho*-dimethoxy-functionalized ligands was implemented to control MOF porosity using the same topology and framework. By judicious choice of ligand ratio, the quantity of adsorption ($N_2$), surface area, and calculated pore volume were controlled after evacuation (*i.e.*, activation of the MOFs). Detailed structural analyses of DMOF-[2,3-$(OMe)_2$] and DMOF-[2,5-$(OMe)_2$] were performed to determine differences in specific properties. In addition, quantum chemical simulation allowed for estimation of the energy differences between the coordination bonds of DMOF-[2,3-$(OMe)_2$] and DMOF-[2,5-$(OMe)_2$].

## EXPERIMENTAL SECTION

### 2.1. Preparation of regioisomeric ligands

Dimethy-2,3-dimethoxyterephthalate and diethy-2,5-dimethoxyterephthalate were prepared following literature procedures (Scheme S1).[11,15]

Dimethyl-2,3-dimethoxyterephthalate (**1a**): Dimethyl-2,3-dihydroxyterephthalate (1.27 g, 5 mmol), potassium carbonate (830 mg, 16 mmol) were dissolved in acetone. Iodomethane (1 mL, 16 mmol) were added to solution, and solution mixture was stirred for overnight under reflux condition. When the reaction was finished (monitored by TLC), organic solvent was evaporated, and then water and EtOAc were added to dissolve all organic molecules and inorganic salts. The solution was three times extracted with EtOAc. The organic layer was dried using anhydrous $MgSO_4$. After filtered off the solid, the solution was evaporated and dried under vacuum. Further purification on flash column chromatograph with *n*-hexane/EtOAc was performed to obtain colorless solid.

Diethyl-2,5-dimethoxyterephthalate (**1b**): Diethyl-2,5-dimethoxyterephthalate was obtained in comparable yield from a similar procedure for **1a**; using diethyl-2,5-dihydroxyterephthalate than

dimethyl-2,3-dihydroxyterephthalate. The colorless solid were obtained after column chromatography.

2,3-Dimethoxyterephthalic acid (**2a**): Dimethyl-2,3-dihydroxyterephthalate (1.02 g, 4 mmol) was dissolved in 20 mL of THF. And 20 mL of a 4% potassium hydroxide aqueous solution was added to THF solution. The solution mixture was stirred overnight under reflux condition. Once conversion was complete (monitored by TLC), THF was removed by evaporation, and the solution was acidified with a 1.0 M HCl aqueous solution to pH 2. The precipitate was collected by filtration and washed with water. The desired compound was obtained colorless solid.

2,5-Dimethoxyterephthalic acid (**2b**): 2,5-Dimethoxyterephthalic acid was obtained in comparable yield from a similar procedure for **2a**; using diethyl-2,5-dimethoxyterephthalate (**1b**) as a starting material. The desired compound was obtained colorless solid.

2.2. Preparation of mixed MOFs

The DMOF series was prepared and activated using a modified method from what has been previously described (Scheme S2).[13,16]

DMOF-[2,3-$(OMe)_2$]: **2a** (89.6 mg, 0.4 mmol) and $Zn(NO_3)_2 \cdot 6H_2O$ (119 mg, 0.4 mmol) were dissolved in 10 mL of DMF (*N,N*-dimethylformamide). To this mixture, DABCO (90 mg, 0.8 mmol) was added and the white precipitate was filtered out with fine porosity disc filter. Then, the clear solution was moved to a scintillation vial (20 mL size) and heated from room temperature to 100 °C (increasing rate = 2.5 °C/min). The temperature was held for 24 h at 100 °C, and then cooled to room temperature (decreasing rate = 2.5 °C/min). The resulting crystals were washed with DMF (5 mL X 3) and chloroform (5 mL X 3). The chloroform solution was replaced with fresh chloroform (5 mL) per 24 h for three cycles. The colorless crystals were obtained after washing and soaked in $CHCl_3$ until usage.

DMOF-[2,5-$(OMe)_2$]: **2b** (89.6 mg, 0.4 mmol) and $Zn(NO_3)_2 \cdot 6H_2O$ (119 mg, 0.4 mmol) were dissolved in 10 mL of DMF. To this mixture, DABCO (90 mg, 0.8 mmol) was added and the white precipitate was filtered out with fine porosity disc filter. Then, the clear solution was moved to a scintillation vial (20 mL size) and heated from room temperature to 100 °C (increasing rate = 2.5 °C/min). The temperature was held for 24 h at 100 °C, and then cooled to room temperature (decreasing rate = 2.5 °C/min). The resulting crystals were washed with DMF (5 mL X 3) and chloroform (5 mL X 3). The chloroform solution was replaced with fresh chloroform (5 mL) per 24 h for three cycles. The colorless crystals were obtained after washing and soaked in $CHCl_3$ until usage.

DMOF-[2,3-$(OMe)_2]_x$[2,5-$(OMe)_2]_y$: The mixed DMOFs were obtained by following similar procedure of [DMOF-2,3-$(OMe)_2$] and DMOF-[2,5-$(OMe)_2$] with ligand mixtures. **2a** and **2b** were mixed with various mole fractions (3:1, 1:1, and 1:3), and then $Zn(NO_3)_2 \cdot 6H_2O$ (119 mg, 0.4 mmol) was added, and the solid mixtures were dissolved in 10 mL of DMF. To this mixture, DABCO (90 mg, 0.8 mmol) was added and the white precipitate was filtered out with fine porosity disc filter. Then, the clear solution was moved to a scintillation vial (20 mL size) and heated from room temperature to 100 °C (increasing rate = 2.5 °C/min). The temperature was held for 24 h at 100 °C, and then cooled to room temperature (decreasing rate = 2.5 °C/min). The resulting crystals were washed with DMF (5 mL X 3) and chloroform (5 mL X 3). The chloroform solution was replaced with fresh chloroform (5 mL) per 24 h for three cycles. The colorless crystals were obtained after washing and soaked in $CHCl_3$ until usage.

## RESULTS AND DISCUSSION

### Synthesis of mixed DMOFs with different ligand ratios and associated porosity changes

In the previous study focusing on the flexibility control of MOFs with functional group regioisomerism,[11–13] the possibility of porosity control of MOFs with a combination of ligands was raised. Electron-rich, dimethoxy functionalization was selected, and Zn-based DMOFs were studied as the main MOF system as it showed a significant flexibility changes based on the regioisomerism.[17] Two main ligands, BDC-2,3-$(OMe)_2$ and BDC-2,5-$(OMe)_2$, were prepared by following previously reported procedures through methylation of dihydroxy ligands (Scheme S1).[13]

Mixed ligand strategies for MOFs are commonly used to introduce multi-functionalities. Various combinations of ligands have been studied for the preparation of mixed MOFs.[18,19] Among them, ligand combinations with the same coordinating ligands but different chemical tags have been extensively studied because they allow for the generation of isoreticular structures from pristine, non-functionalized, or single-functionalized MOFs. For example, mixed UiO-66-$(NH_2)_x(Br)_y$ (x+y =1) were simply prepared using a mixed ligand solution of BDC-$NH_2$ and BDC-Br, exhibiting the same framework as those of UiO-66, UiO-66-$NH_2$, and UiO-66-Br.[20] Therefore, a series of ratio-controlled mixtures of BDC-2,3-$(OMe)_2$ and BDC-2,5-$(OMe)_2$ allowed for identical MOF structures with completely different porosities.

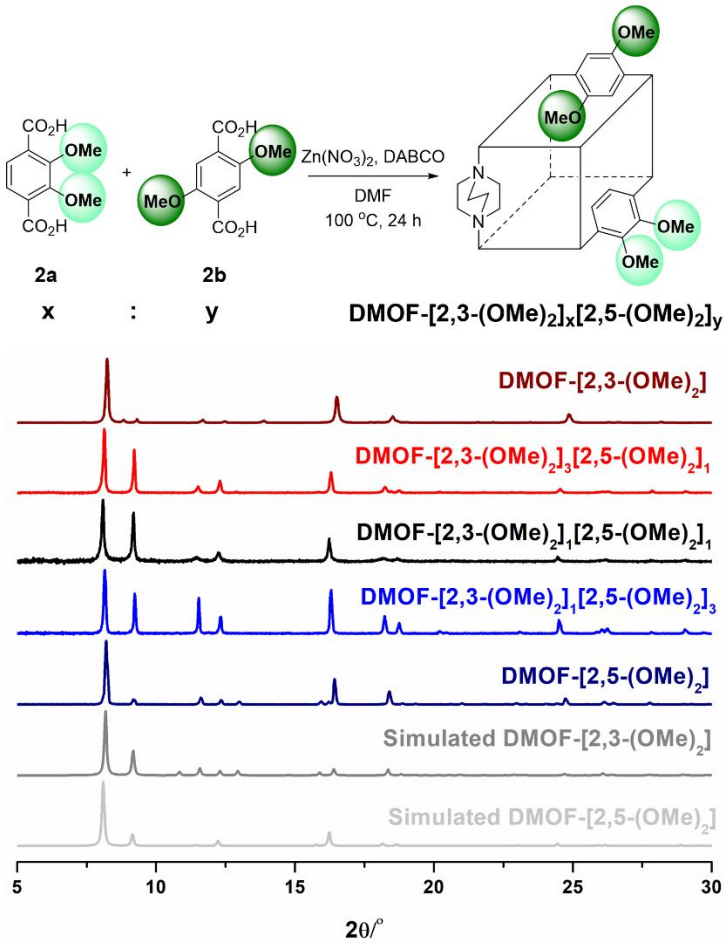


**Figure 1**. Synthesis of mixed DMOFs with BDC-2,3-$(OMe)_2$ and BDC-2,5-$(OMe)_2$ and their associated PXRD patterns (as-synthesized) and simulated PXRD patterns (for DMOF-[2,3-$(OMe)_2$] and DMOF-[2,5-$(OMe)_2$].

Using a series of dimethoxy-functionalized ligands, Zn(II)-based DMOFs were synthesized (Figure 1 and Scheme S2). DMOF-[2,3-$(OMe)_2$], DMOF-[2,3-$(OMe)_2]_3$[2,5-$(OMe)_2]_1$, DMOF-[2,3-$(OMe)_2]_1$[2,5-$(OMe)_2]_1$, DMOF-[2,3-$(OMe)_2]_1$[2,5-$(OMe)_2]_3$, and DMOF-[2,5-$(OMe)_2$] were prepared by combining the appropriate ligand mixture with DABCO in DMF, and heating the mixture to 100 °C for 24 h. Crystalline ratio-controlled DMOFs exhibited the framework that was identical to that of the parent DMOF-1, as evidenced by the PXRD pattern (Figure 1). The $^1$H

NMR spectra after acid digestion (with DCl in $D_2O$) of the DMOFs showed that the ratio of BDC-2,3-$(OMe)_2$ and BDC-2,5-$(OMe)_2$ from the solution mixture was completely retained in all DMOFs. In addition, for the 2:1 ratio between the BDCs and $Zn(NO_3)_2$, the DABCO ligands were confirmed for all samples (Figure S1). Although the ratios between the two regioisomers were well matched at the bulk level, a detailed NMR analysis was additionally performed to confirm the homogeneity of MOF crystals with two different ligands. A large single crystal of DMOF-[2,3-$(OMe)_2]_1$[2,5-$(OMe)_2]_1$ (<2 mm in size) was selected, and the $^1$H NMR spectra (from overnight measurement) after acid digestion clearly showed two significant signals arising simultaneously from two regioisomeric ligands (Figure S2). Therefore, it was clearly confirmed that the combinations of regioisomeric ligands with different functional group positions were compatible with the proposed DMOF synthesis.

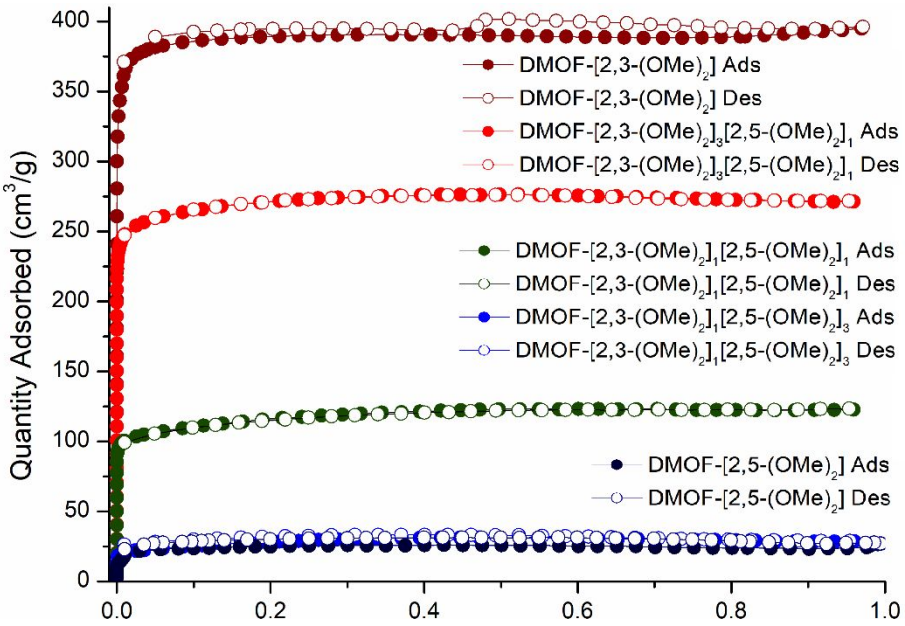


**Figure 2.** $N_2$ full isotherms (77 K) of the obtained mixed DMOFs from the regioisomeric ligand mixtures.

Gas adsorption experiments with $N_2$ (at 77 K) were performed to confirm the porosity of the mixed DMOFs. Previously, electron-rich DMOF with a *para*-position group such as DMOF-[2,5-$(OMe)_2$] showed almost non-porous properties after evacuation, indicating a flexible framework. The Brunauer-Emmett-Teller (BET) surface area of DMOF-[2,5-$(OMe)_2$] was 73 $m^2/g$, while the *ortho*-regioisomer DMOF-[2,3-$(OMe)_2$] was highly porous after evacuation, indicating an inflexible framework (BET surface area = 1554 $m^2/g$; Figure S3).[13] Although both DMOF-[2,3-$(OMe)_2$] and DMOF-[2,5-$(OMe)_2$] contained identical frameworks in the as-synthesized state, their porosity was totally changed from highly porous to non-porous by moving the relative position of the functional group.[13] Interestingly, the DMOF porosity was generally controllable by mixing of the two regioisomeric ligands. The equivalent-proportioned DMOF-[2,3-$(OMe)_2$]$_1$[2,5-$(OMe)_2$]$_1$ obtained using a 1:1 ligand mixture of BDC-2,3-$(OMe)_2$ and BDC-2,5-$(OMe)_2$ showed moderate porosity (~120 $cm^3/g$ adsorbed at STP), micropore volume (329 $cm^3/g$), and BET surface area (437 $m^2/g$; Figures 2 and S3–S6). In addition, the sample prepared using a 3:1 ratio of BDC-2,3-$(OMe)_2$ to BDC-2,5-$(OMe)_2$ showed a highly porous structure (1057 $m^2/g$ BET surface area), but lower porosity than that of pure DMOF-[2,3-$(OMe)_2$] (Figures 2 and S4). Finally, the sample prepared using a 1:3 ratio of BDC-2,3-$(OMe)_2$ to BDC-2,5-$(OMe)_2$ displayed almost non-porous properties; however, it was slightly more porous than pure DMOF-[2,5-$(OMe)_2$] (Figures 2 and S6). All ratio-controlled DMOFs showed identical frameworks as the as-synthesized form (as indicated by the PXRD patterns; Figure 1), but showed completely different porosities, as indicated by $N_2$ adsorption after evacuation (Table S1; micropore volume). Moreover, gas adsorption experiments with $CO_2$ (at 298 K) were performed to confirm the porosity changes of the mixed DMOFs and determine the flexibility of the molecular interactions (Figure S7). Not surprisingly, DMOF-[2,3-$(OMe)_2$] showed the highest $CO_2$ uptake, while DMOF-[2,5-$(OMe)_2$] displayed the

lowest uptake for $CO_2$ at 298 K. Thus, no differences between DMOF-$N_2$ and DMOF-$CO_2$ interactions were observed owing to structural changes induced by regioisomerism. Furthermore, the $CO_2$ uptake was controlled by mixed-regioisomeric DMOFs (0.25–3.75 mmol/g; Figure S7).

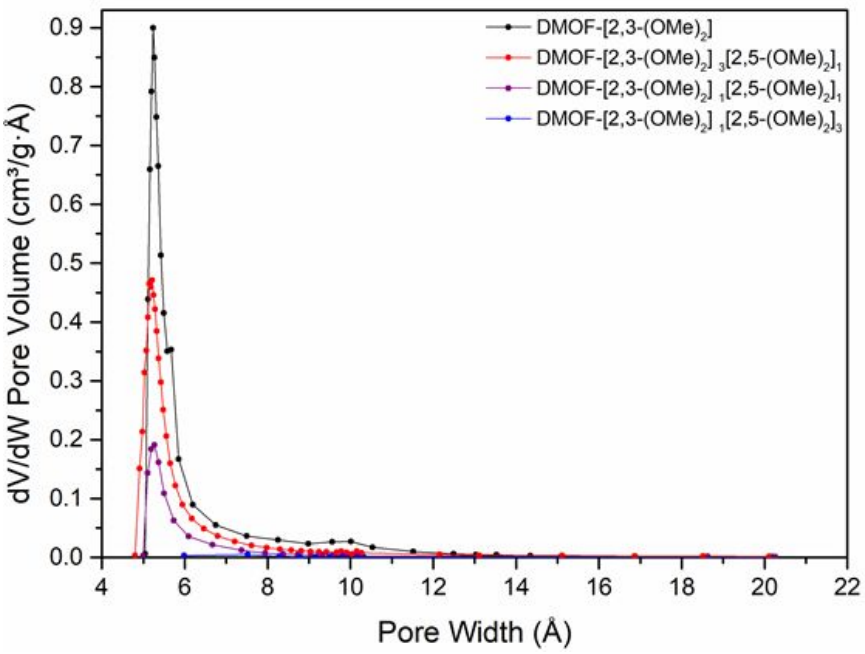


**Figure 3.** Pore size distribution of the mixed-regioisomeric DMOFs using the H-K method for micropore analysis.

The porous properties of the DMOFs were evaluated using BET surface area, total pore volume, and pore size distribution (PSD; Table S1). The BET surface area is a good measure of the size of accessible empty space. However, PSD provides insight into the pore size, shape, and population changes within the DMOFs. The PSD differ depending on the calculation method. Therefore, the PSD calculated by the NLDFT (Non-Linear Density Function Theory) method assuming cylindrical pore geometry incorporated in an ASAP2020 gas sorption instrument was first plotted[21,22] to provide information regarding the pore size distribution over a wide range—from micro- to macropores (Figure S8). The PSD determined using the NLDFT method demonstrated

that no meso- and macropores were present in the prepared DMOF, indicating that a PSD method for micropores should be used, such as the Horváth-Kawazoe (H-K) model.[23] The PSD of the DMOF calculated using the H-K model assuming a narrow cylindrical pore geometry is presented in Figure 3 focusing on the micropore range (0–20 Å).[24] The average pore size was ~ 5.4 Å regardless of the 2,3- and 2,5-OMe ligand ratio. However, the pore volume corresponding to the largest pore occupying size decreased with increasing 2,5-OMe ligand ratio. The PSD results clearly indicate that the decreased surface area is not derived from pore size and shape changes in the DMOFs, but originates from the decrease in the number (or volume) of the accessible pores. Therefore, increasing the 2,5-OMe ligand content allows for the generation of a greater amount of non-accessible small pores in the DMOF, resulting in an accessible pore volume decrease without a significant pore size change.

Because the gas adsorption experiments were conducted with fully evacuated samples (*i.e.*, activated samples with empty pores), the structural changes caused by evacuation were monitored by PXRD after vacuum drying. Interestingly, only the most non-porous DMOF-[2,5-$(OMe)_2$] showed a significant peak shift to a higher angle, indicating structural changes from large pores (*lp*) to narrow pores (*np*). This structural change was not reversible as the as-synthesized status was not recovered after re-solvation with either $CHCl_3$ or DMF. Other mixed DMOFs and porous DMOF-[2,3-$(OMe)_2$] exhibited no peak shift in the PXRD data upon evacuation (Figure S9). The mixed-regioisomeric DMOFs were instantly decomposed during the PXRD measurements. Therefore, only several broad peaks at low angles were confirmed; however, detailed structural information of the fully dried DMOFs was not obtained by PXRD and single X-ray diffraction data (SXRD). For the flexible-irreversible DMOF-[2,5-$(OMe)_2$], similar PXRD peak shifts upon evacuation were observed in a previous study with other flexible DMOFs, DMOF-2,5-$NH_2Cl$, and

DMOF-2,5-$NH_2$Br.[11] In addition, the PXRD peak shifts upon evacuation from the *lp* to *np* phases (~1° in 2θ) are very similar for three electron-rich DMOFs with *para*-functionalizations (evacuated DMOF-[2,5-$(OMe)_2$] vs. evacuated DMOF-2,5-$NH_2$Cl and DMOF-2,5-$NH_2$Br; Figure S9).[11]

This structural transformation from *lp* to *np* is likely the main factor for porosity control. The additional inclusion of electron-rich ligands (*e.g.*, BDC-2,5-$(OMe)_2$) could induce a more collapsed framework compared to the pristine electron-deficient MOFs (*e.g.*, DMOF-[2,3-$(OMe)_2$]), with the related porosity changes upon evacuation. These structural transformations of mixed-regioisomeric DMOFs can occur simultaneously for a whole crystal or during the partial collapse of specific crystal domains. Since detailed structural evaluation after evacuation is rather challenging, high-level computational approaches must be performed to understand the structural transformation mechanisms in infinite frameworks. Not surprisingly, thermogravimetry analysis (TGA) showed no significant changes as a function of regioisomeric ligand ratios for a series of DMOF-$[2,3\text{-}(OMe)_2]_x[2,5\text{-}(OMe)_2]_y$ (x or y = 0, 1, and 3; Figure S10).

**Structural differences between DMOF-[2,3-$(OMe)_2$] and DMOF-[2,5-$(OMe)_2$]**

To determine the porosity changes of a series of mixed DMOFs prepared using different regioisomeric ligands, the structural differences between the DMOF regioisomers, DMOF-[2,3-$(OMe)_2$] and DMOF-[2,5-$(OMe)_2$], were carefully evaluated *via* SXRD (Figures 4, S11, Tables S2–S10, and Cambridge Crystallographic Data Centre Deposit# 1994998-1995002). Generally, both DMOF-[2,3-$(OMe)_2$] and DMOF-[2,5-$(OMe)_2$] adopted similar structures over the entire framework. Dinuclear zinc units formed paddle-wheel type nodes, and this SBU was bridged by BDC-$(OMe)_2$ ligands to form a distorted 2-dimensional square-grid (*i.e.*, $Zn_2$(BDC-$(OMe)_2)_2$). Two axial positions of $Zn_2$ SBU were contained two DABCO molecules as pillar ligands to

configure 3-dimensional frameworks from 2-dimensional sheets. The overall structure of both DMOF-[2,3-$(OMe)_2$] and DMOF-[2,5-$(OMe)_2$] were identical to the previously reported DMOF-1 structure prepared from the non-functionalized BDC ligand,[14] but the detailed coordination environments between the dimeric paddle-wheel SBU and BDC ligands differed significantly in terms of methoxy group position. First, the disorder of dimethoxy functional groups displayed different behaviors for regioisomeric DMOFs. For the *ortho*-functionalized DMOF-[2,3-$(OMe)_2$], the position of the dimethoxy group was fixed, and two methoxy groups were directed into the inside of the square. Simultaneously, the other two methoxy groups pointed toward the outside of the 2-dimensional square (Figure 4a). In contrast, all methoxy groups were disordered in the *para*-functionalized DMOF-[2,5-$(OMe)_2$] (Figure 4b).

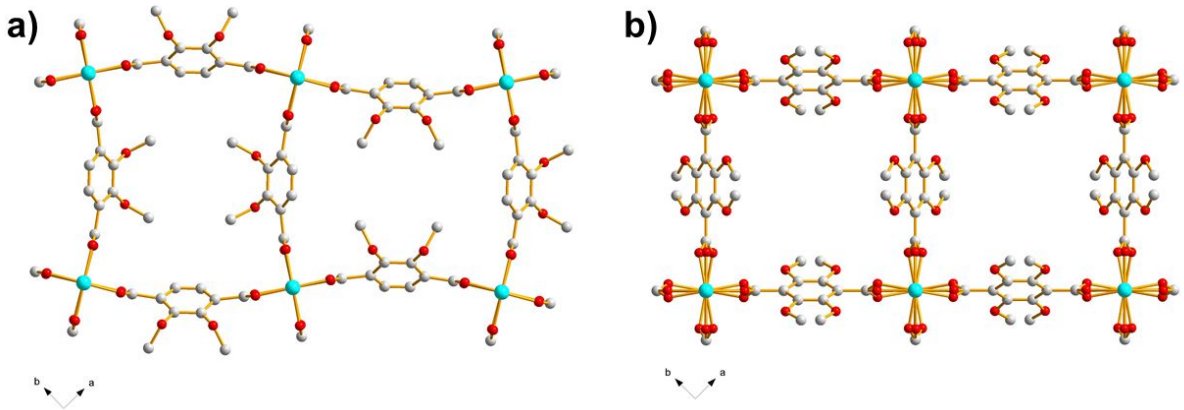


**Figure 4.** Structural differences observed in the SXRD data of DMOF-[2,3-$(OMe)_2$] (a, left) and DMOF-[2,5-$(OMe)_2$] (b, right). Because of the disorder of the substituents on the BDC-2,5-$(OMe)_2$ ligand, the methoxy groups were refined as disordered over the 2, 3, 5, and 6 positions of the benzene ring. Color scheme: Zn (cyan), O (red), C (gray), and N (blue).

In addition, the overall balances of the whole structures were distinguished by the relative positions of the methoxy groups. While the 2-dimensional sheet from the top view formed exact

square-type pores in the net structure of DMOF-[2,5-$(OMe)_2$], the 2-dimensional squares from the top view of DMOF-[2,3-$(OMe)_2$] were slightly squeezed, and the two-crossed vertically enlarged/horizontally enlarged squares repeated over the entire 2-dimensional sheet. Moreover, coordination between the zinc cation and carboxylate was also distinct for the two regioisomeric DMOFs. The coordination bonds in the *para*-functionalized DMOF-[2,5-$(OMe)_2$] showed fluctuating characteristics, especially the Zn–O bonds that were completely disordered. In contrast, DMOF-[2,3-$(OMe)_2$] displayed a single position for the Zn–O bond for all coordination bonds in the framework. Therefore, to maintain balance over the entire framework, the ligand was bent to an arrow type to the inside and outside of the pore (Figures 4 and S11). The Zn-BDC-Zn angle in the *ortho*-DMOF was 164°, while the *para*-functionalized DMOF-2,5-$(OMe)_2$ showed a perfectly flat 180° angle (Figure S12). We assumed that this discrepancy originated from differences in the coordination bond strengths of the DMOFs. The coordination bonds between $Zn^{2+}$ and BDC-2,3-$(OMe)_2$ are much stronger than the coordination bond between $Zn^{2+}$ and BDC-2,5-$(OMe)_2$. Therefore, the Zn-O coordination bonds in DMOF-[2,3-$(OMe)_2$] were completely maintained in a single position of the X-ray structure, retaining the original pore size of DMOF-[2,3-$(OMe)_2$] (*i.e.*, porosity to $N_2$ after evacuation). In contrast, the weaker coordination bonds of DMOF-[2,5-$(OMe)_2$] were disordered in the associated X-ray structures, and adopted a narrow pore size upon evacuation. Finally, the crystal structures of the regiomixtures, DMOF-[2,3-$(OMe)_2]_3$[2,5-$(OMe)_2]_1$, DMOF-[2,3-$(OMe)_2]_1$[2,5-$(OMe)_2]_1$, and DMOF-[2,3-$(OMe)_2]_1$[2,5-$(OMe)_2]_3$ were analyzed using SXRD data. Interestingly, all three mixtures displayed almost identical structures to that of DMOF-[2,5-$(OMe)_2$] (Figure S13). The structural rigidity of DMOF-[2,3-$(OMe)_2$] was only observed for the pure DMOF from BDC-2,3-$(OMe)_2$, strongly suggesting that the disorder

characteristics of coordination bonds from the *para*-functionalized BDC-2,5-$(OMe)_2$ were dominant over the *ortho*-functionalized ligand.

**Quantum chemical simulations to examine differences in coordination between regioisomeric mixtures**

Quantum chemical simulations were performed to examine the coordination environment differences between regioisomeric MOFs with dimethoxy-functionalities. It is not appropriate to use quantum chemistry to investigate entire MOF particles with a nearly infinite 3D matrix-like structure. As discussed previously,[17] rationally truncated cluster model structures can instead be used to generally understand and describe the electronic and geometric features of entire MOFs. The cluster model has been widely used to investigate MOF properties such as spin property,[25] hydrogen gas adsorption,[26] and photophysical properties.[27] The cluster model structures incorporated two Zn divalent ions coordinated by four BDC-$(OMe)_2$ anion ligands (*ortho*- and *para*-functionalized BDCs), which were capped by two neutral DABCOs (*e.g.*, $Zn_2$(BDC-2,3-$(OMe)_2)_4(DABCO)_2$ and $Zn_2$(BDC-2,5-$(OMe)_2)_4(DABCO)_2$). The formula of these clusters are identical to the well-known molecular formula of Zn-based MOFs (*e.g.*, $Zn_2(BDC)_2(DABCO)$). Four conformers are possible depending on the relative orientation of the methoxy groups in neighboring BDCs for each model, and all possible conformers were considered in the simulations. This simplified cluster model is useful for obtaining insight into the chemical interactions between the BDC-$(OMe)_2$ ligands and two divalent Zn ions. The lowest-energy structures were determined by density functional theory (DFT) with the $\omega$B97X-D functional. The double-zeta with polarization functions, 6-31G* basis sets were employed for describing light atoms (H, C, N, and

O), whereas LANL2DZ ECP and its corresponding basis sets were used to compute the Zn atoms. All quantum chemical simulations were performed using Q-Chem 5.2.[28]

We predicted four energetic minima for each model structure using the DFT approach. Two of the four model structures of $Zn_2$(BDC-2,5-$(OMe)_2)_4(DABCO)_2$ were excluded from the analysis because of strong π-π interactions between two adjacent BDCs that are not present over the entire MOF framework. Because of truncation and use of simplified models, which include only one SBU, BDC ligands gain artificial freedom to rearrange, which is not possible in the real MOF structures. This implies that caution must be exercised when the approximate simplified model is used to represent nearly infinite 3D framework-type structures. The global minimum-energy geometry of $Zn_2$(BDC-2,3-$(OMe)_2)_4(DABCO)_2$ does not include such unrealistic interactions. The ground state geometries of the two model structures, the third lowest-energy structure of $Zn_2$(BDC-2,3-$(OMe)_2)_4(DABCO)_2$ and lowest-energy structure of $Zn_2$(BDC-2,5-$(OMe)_2)_4(DABCO)_2$, determined by DFT geometry optimizations are shown in Figure 5 (Figures S14 and S15).

| Isomer | Side view | Top view |
|---|---|---|
| 2,3-$(OMe)_2$ | 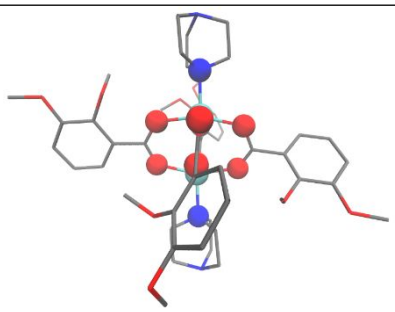 | 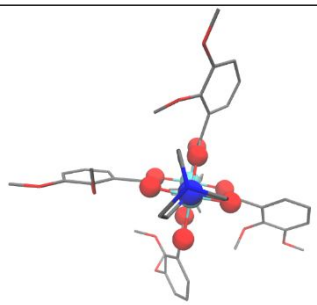 |
| 2,5-$(OMe)_2$ | 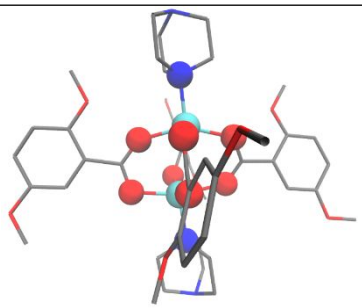 | 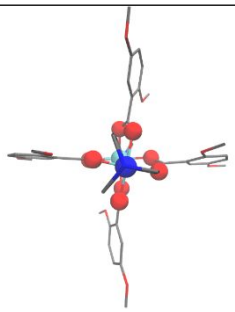 |

**Figure 5.** The predicted ground state geometries of the model systems, $Zn_2$(BDC-2,3-$(OMe)_2)_4(DABCO)_2$ and $Zn_2$(BDC-2,5-$(OMe)_2)_4(DABCO)_2$. The atoms directly connected to the metal ions are described with a ball-and-stick model, while other atoms are described with a simple line model. Hydrogen atoms were removed for clarity. Color scheme: Zn (cyan), O (red), C (gray), and N (blue).

The general shape of the optimized models includes two square pyramids with $Zn^{2+}$ placed at the center. Deviation from an octahedral-like structure for a zinc central atom has also been reported in previously,[17] and a similar geometric distortion was observed for the two model structures studied herein. In the optimized model structures, the *ortho*-functionalized BDC-2,3-$(OMe)_2$ ligands have two methoxy groups placed at the same side causing severe steric hindrance, resulting in methoxy groups perpendicular to a benzene ring on BDC. However, the methoxy groups in the *para*-functionalized BDC-2,5-$(OMe)_2$ ligands do experience such crowdedness and retain planar structures. This difference in methoxy orientation affects the relative arrangement and position of the two square pyramid structures.

The dominant interaction between zinc cations and carboxylic anions is the electrostatic term. This indicates that other interactions could be adjusted to maximize Coulombic attraction. The methoxy groups perpendicular to an *ortho*-functionalized BDC-2,3-$(OMe)_2$ ring induced an asymmetric $\angle C_{BDC}$-$O_{BDC}$-Zn angle to relieve the steric hindrance between the methoxy groups and DABCO while maintaining sizable electrostatic attractions ($X_{BDC}$ is an X atom in the BDC ligand). This asymmetric carboxyl coordination was appreciably observed where the two $\angle C_{BDC}$-$O_{BDC}$-Zn angles are 167° and 96° in one BDC ligand, and 153° and 104° for the other BDC ligand in the cluster (Figure S16). Therefore, the centers of the two square pyramids deviated significantly from each other, as quantified using the two angles formed by $\angle N_{DABCO}$-$Zn_1$-$Zn_2$ (152° and 160°,

respectively; Figure S16). This structural feature indicates that the two square pyramids in the cluster are slipped stacked in the *ortho*-functionalized BDC-2,3-$(OMe)_2$. From this displacement, the $O_{BDC}$ belonging to the other square pyramid is shifted closer to the Zn ions (2.40 Å and 2.66 Å compared to the inoperative ones of 3.3 and 3.4 Å), and the coordination environment near Zn is similar to a 5+1 configuration (four close $O_{BDC}$, one $N_{DABCO}$, and one distant $O_{BDC}$). This provides extra interaction between distant $O_{BDC}$ and Zn in addition to the four strongly bound in its square pyramids (Sideview of cluster in Figure 5). However, in the $Zn_2$(BDC-2,5-$(OMe)_2)_4(DABCO)_2$ model structures, where BDC ligands experience much less steric hindrance, marginal impacts on the interaction between Zn cations and carboxylic anions were observed. The centers of the two square pyramids are nearly in line (*i.e.*, $\angle N_{DABCO}$-$Zn_1$-$Zn_2$ = 165°; Figure S17), and no additional distant $O_{BDC}$ coordination was observed in the *para*-functionalized $Zn_2$(BDC-2,5-$(OMe)_2)_4(DABCO)_2$ model structures.

Using these optimized structures, the binding energy was defined as E[$Zn_2$(BDC-2,n-$(OMe)_2)_4(DABCO)_2$]–4×E[BDC-2,n-$(OMe)_2)_4^-$]–E[$Zn_2(DABCO)_2^{4+}$], where n is either 3 or 5 (E[X] is the electronic energy of chemical species X). Electronic energy was obtained from DFT geometry optimizations. This calculation yielded a binding energy of 133.7 kcal/mol for the *ortho*-functionalized $Zn_2$(BDC-2,3-$(OMe)_2)_4(DABCO)_2$ model and 125.2 kcal/mol for the *para*-functionalized $Zn_2$(BDC-2,5-$(OMe)_2)_4(DABCO)_2$ model. This indicated indicates that the *ortho*-functionalized BDC-2,3-$(OMe)_2$ ligands were more strongly bound to the $Zn^{2+}$ ions than the *para*-functionalized BDC-2,5-$(OMe)_2$. This can be understood based on the structural features of the extra interaction between the $Zn^{2+}$ and distant $O_{DBC}$ (see above). The binding energy analysis performed *via* quantum chemical simulations supported and explained the different porosities observed for the mixed DMOFs after the blending of the two regioisomeric BDC-2,3-$(OMe)_2$ and

BDC-2,5-$(OMe)_2$ ligands after evacuation under vacuum. The more strongly coordinated *ortho*-functionalized BDC-2,3-$(OMe)_2$ ligands were more resistant to external pressure and stimuli. The small structural changes in the relative orientation of substituents at the molecular level could affect the properties of the metal-ligand clusters and entire MOF framework, resulting in different macroscopic behavior at the experimental level.

## CONCLUSION

Porosity control of pillared DMOFs was achieved using a ligand-blending strategy with BDC-2,3-$(OMe)_2$ and BDC-2,5-$(OMe)_2$ regioisomers. The correlation between the functional group position and structural flexibility has been revealed *via* electron-density-controlled BDC ligands and DMOFs. For electron-rich BDC ligands, functional group regioisomerism allowed for different degrees of flexibility. Pure DMOF-[2,3-$(OMe)_2$] showed highly porous properties (~300 $cm^2/g$ absorbed $N_2$) at 1 atm after evacuation, while pure DMOF-[2,5-$(OMe)_2$] adopted an almost non-porous structure toward $N_2$. The ligand ratio of the *ortho*- and *para*-functionalized ligands resulted in a moderate porosity of the resulting DMOFs. Although all the mixed DMOFs with different ligand ratios showed identical structures in the as-synthesized state, as evidenced by PXRD pattern analysis, the porosity of the mixed DMOFs varied with the ligand ratio from non-porous to highly porous. When a 1:1 ratio of the two regioisomeric ligands was incorporated into the DMOFs, the average porosity obtained fell in between the two pure DMOF-$(OMe)_2$s. When the *ortho*-functionalized BDC-2,3-$(OMe)_2$ was more abundant that of the *para*-functionalized ligand, the resulting DMOF-$[2,3\text{-}(OMe)_2]_3[2,5\text{-}(OMe)_2]_1$ displayed higher porosity than the 1:1 ligand mixture.

Detailed structural analysis was performed to examine differences between the regioisomeric functional groups and associated porosity changes. Although the two regioisomeric DMOFs, DMOF-[2,3-$(OMe)_2$] and DMOF-[2,5-$(OMe)_2$], are identical except for the ligand positions, the coordination environments were slightly different in the X-ray structures. Interestingly, the *ortho*-functionalized DMOF-[2,3-$(OMe)_2$] showed more rigid coordination bonds between the $Zn^{2+}$ and carboxylate in BDC compared to those in DMOF-[2,5-$(OMe)_2$]. Therefore, the overall structural balance of the frameworks was modulated by the bending motion of the ligand in the *ortho*-functionalized DMOF-[2,3-$(OMe)_2$]. In contrast, the twisting motion of SBU adjusted the structural balance of the frameworks in DMOF-[2,5-$(OMe)_2$] because the coordination of DMOF-[2,5-$(OMe)_2$] is much weaker than that of DMOF-[2,3-$(OMe)_2$]. These structural findings are well correlated with the experimental $N_2$ adsorption results. The coordination bond differences between *ortho*- and *para*-functionalized dimethoxy ligands induced porosity changes upon evacuation.

Finally, quantum chemical simulations were performed to understand the binding differences between *ortho*- and *para*-dimethoxy-functionalized ligands. While BDC ligands experience much less steric hindrance in the $Zn_2$(BDC-2,5-$(OMe)_2)_4(DABCO)_2$ model structures, the methoxy groups perpendicular to the BDC-2,3-$(OMe)_2$ ring induced an asymmetric $\angle C_{BDC}$-$O_{BDC}$-Zn angle to relieve steric hindrance between the methoxy groups and DABCO while maintaining sizable electrostatic attractions. Therefore, the center of the two square pyramids in the vertex of the DMOF structure significantly deviated. Additionally, these differences in the optimized structures were successfully utilized for binding energy comparisons. This calculation gave a binding energy of 133.7 kcal/mol for the *ortho*-functionalized $Zn_2$(BDC-2,3-$(OMe)_2)_4(DABCO)_2$ model and 125.2 kcal/mol for the *para*-functionalized $Zn_2$(BDC-2,5-$(OMe)_2)_4(DABCO)_2$ model, indicating that the *ortho*-functionalized BDC-2,3-$(OMe)_2$ ligands are more strongly bound to $Zn^{2+}$. The more

strongly coordinated *ortho*-functionalized BDC-2,3-$(OMe)_2$ ligands were more resistant to external pressure and stimuli.

In summary, MOF porosity could be controlled by a ligand-mixing strategy with regioisomeric ligands. Although the chemical formula and as-synthesized structures are identical, the porosities upon evacuation varied and were controllable by adjusting the ligand ratio. The detailed structural analysis using X-ray crystallography and quantum chemical simulation revealed important differences in the coordination environment between the zinc ion and carboxylate ligand for the *ortho*- and *para*-regioisomers. The small structural change in the relative orientation of substituents at the molecular level affected the properties of the metal-ligand clusters and the entire MOF framework, resulting in different macroscopic behavior.

AUTHOR INFORMATION

**Corresponding Author**

Minyoung Yoon, Department of Chemistry, Kyungbook National University, Daegu, 41566, Korea, *E-mail: myyoon@knu.ac.kr (M. Yoon)

Hyungjun Kim, Department of Chemistry, Incheon National University, Incheon, 22012, Korea, *E-mail: kim.hyungjun@inu.ac.kr (H. Kim)

Dongwook Kim, Center for Catalytic Hydrocarbon Functionalization, Institute of Basic Science, *E-mail: dwkxtal@kaist.ac.kr (D. Kim)

Min Kim, Department of Chemistry, Chungbuk National University, Cheongju, 28644, Korea, *E-mail: minkim@chungbuk.ac.kr (M. Kim)

**Authors**

Dopil Kim – Department of Chemistry, Chungbuk National University, Cheongju, 28644, Korea

Hyeonbin Ha –Department of Chemistry, Chungbuk National University, Cheongju, 28644, Korea

Youngik Kim – Department of Chemistry, Chungbuk National University, Cheongju, 28644, Korea

Younghu Son – Department of Chemistry, Kyungbook National University, Daegu, 41566, Korea

Jiyoon Choi – Department of Chemistry, Incheon National University, Incheon, 22012, Korea

Myung Hwan Park – Department of Chemistry Education, Chungbuk National University, Cheongju, 28644, Korea

Youngjo Kim – Department of Chemistry, Chungbuk National University, Cheongju, 28644, Korea

**Author Contributions**

[#]D. Kim and H. Ha contributed equally to this work.

**Notes**

The authors declare no competing financial interest.

ACKNOWLEDGMENT

This research was supported by the Basic Science Research Program (2019R1A2C4070584) and the Science Research Center (2016R1A5A1009405) through the National Research Foundation of

Korea (NRF) funded by the Ministry of Science and ICT. Single crystal and powder X-ray diffraction experiments at PLS-II, 2D-SMC beamlines were supported in part by MSIT and POSTECH. H. Ha (Ph. D. Student) was supported by Basic Science Research Program (2019R1A6A3A13095922) through the NRF funded by the Ministry of Education. Jiyoon Choi and Hyungjun Kim was supported by the Basic Science Research Program (2017R1A6A1A06015181) through the NRF funded by the Ministry of Educations.

## ASSOCIATED CONTENT

**Supporting Information**.

Synthetic details; NMR spectra; single crystal data; full isotherm data; powder XRD data; TGA data; additional images from computational approaches (PDF)

Accession Codes: CCDC 1994998-1995002 contain the supplementary crystallographic data for this paper. These data can be obtained free of charge *via* www.ccdc.cam.ac.uk/data_request/cif, or by e-mailing data_request@ccdc.cam.ac.kr, or by contacting The Cambridge Crystallographic Data Centre, 12 Union Road, Cambridge, CB2 1EZ, UK; fax +44-1223-336033.

This information is available free of charge *via* the Internet at http://pubs.acs.org/

## REFERENCES

(1) Zhou, H.-C.; Long, J. R.; Yaghi, O. M. Introduction to Metal–Organic Frameworks. *Chem. Rev.* **2012**, *112*, 673–674.

(2) Murray, L. J.; Dincă, M.; Long, J. R. Hydrogen Storage in Metal–Organic Frameworks. *Chem. Soc. Rev.* **2009**, *38*, 1294–1314.

(3) Li, J.-R.; Kuppler, R. J.; Zhou, H.-C. Selective Gas Adsorption and Separation in Metal–Organic Frameworks. *Chem. Soc. Rev*. **2009**, *38*, 1477–1504.

(4) Lee, J.; Farha, O. K.; Roberts, J.; Scheidt, K. A.; Nguyen, S. T.; Hupp, J. T. Metal–Organic Framework Materials as Catalysts. *Chem. Soc. Rev*. **2009**, *38*, 1450–1459.

(5) MacGillivray, L. R.; Lukehart, C. M. *Metal-Organic Framework Materials*; Wiley; Hoboken, NJ, USA, 2014.

(6) Yaghi, O. M.; O'Keeffe, M.; Ockwig, N. W.; Chae, H. K.; Eddaoudi, M.; Kim, J. Reticular Synthesis and the Design of New Materials. *Nature* **2003**, *423*, 705–714.

(7) Nouar, F.; Devic, T.; Chevreau, H.; Guillou, N.; Gibson, E.; Clet, G.; Daturi, M.; Vimont, A.; Grenèche, J. M.; Breeze, M. I.; Walton, R. I.; Llewellyn, P. L.; Serre, C. Tuning the Breathing Behaviour of MIL-53 by Cation Mixing. *Chem. Commun*. **2012**, *48*, 10237–10239.

(8) Cohen, S. M. Postsynthetic Methods for the Functionalization of Metal-Organic Frameworks. *Chem. Rev.* **2012**, *112*, 970–1000.

(9) Klein, N.; Hoffmann, H. C.; Cadiau, A.; Getzschmann, J.; Lohe, M. R.; Paasch, S.; Heydenreich, T.; Adil, K.; Senkovska, I.; Brunner, E.; Kaskel, S. Structural Flexibility and Intrinsic Dynamics in the $M_2(2,6\text{-Ndc})_2(\text{Dabco})$ (M = Ni, Cu, Co, Zn) Metal-Organic Frameworks. *J. Mater. Chem*. **2012**, *22*, 10303–10312.

(10) Schneemann, A.; Bon, V.; Schwedler, I.; Senkovska, I.; Kaskel, S.; Fischer, R. A. Flexible Metal–Organic Frameworks. *Chem. Soc. Rev.* **2014**, *43*, 6062–6096.

(11) Kim, M.; Boissonnault, J. A.; Dau, P. V.; Cohen, S. M. Metal-Organic Framework Regioisomers Based on Bifunctional Ligands. *Angew. Chem., Int. Ed*. **2011**, *50*, 12193–12196.

(12) Hahm, H.; Yoo, K.; Ha, H.; Kim, M. Aromatic Substituent Effects on the Flexibility of Metal–Organic Frameworks. *Inorg. Chem*. **2016**, *55*, 7576–7581.

(13) Ha, H.; Hahm, H.; Jwa, D. G.; Yoo, K.; Park, M. H.; Yoon, M.; Kim, Y.; Kim, M. Flexibility in Metal–Organic Frameworks Derived from Positional and Electronic Effects of Functional Groups. *CrystEngComm* **2017**, *19*, 5361–5368.

(14) Dybtsev, D. N.; Chun, H.; Kim, K. Rigid and Flexible: A Highly Porous Metal–Organic Framework with Unusual Guest-Dependent Dynamic Behavior. *Angew. Chem., Int. Ed*. **2004**, *43*, 5033–5036.

(15) Heldmann, C.; Schulze, M.; Wegner, G. Rigid-Rod-like Main Chain Polymers with Rigidly Attached Chromophores. A Novel Structural Concept for Electrooptical Materials. 1. Synthesis and Characterization. *Macromolecules* **1996**, *29*, 4686–4696.

(16) Wang, Z.; Tanabe, K. K.; Cohen, S. M. Accessing Postsynthetic Modification in a Series of Metal-Organic Frameworks and the Influence of Framework Topology on Reactivity. *Inorg. Chem*. **2009**, *48*, 296–306.

(17) Ha, H.; Kim, Y.; Kim, D.; Lee, J.; Song, Y.; Kim, S.; Park, M. H.; Kim, Y.; Kim, H.; Yoon, M.; Kim, M. Effect of the Metal within Regioisomeric Paddle-Wheel-Type Metal–Organic Frameworks. *Chem. Eur. J*. **2019**, *25*, 14414–14420.

(18) Burrows, A. D. Mixed-Component Metal-Organic Frameworks (MC-MOFs): Enhancing Functionality through Solid Solution Formation and Surface Modifications. *CrystEngComm* **2011**, *13*, 3623–3642.

(19) Abednatanzi, S.; Gohari Derakhshandeh, P.; Depauw, H.; Coudert, F. X.; Vrielinck, H.; Van Der Voort, P.; Leus, K. Mixed-Metal Metal-Organic Frameworks. *Chem. Soc. Rev.* **2019**, *48*, 2535–2565.

(20) Kim, M.; Cahill, J. F.; Prather, K. A.; Cohen, S. M. Postsynthetic Modification at Orthogonal Reactive Sites on Mixed, Bifunctional Metal-Organic Frameworks. *Chem. Commun*. **2011**, *47*, 7629–7631.

(21) Tarazona, P.; Marini Bettolo Marconi, U.; Evans, R. Phase Equilibria of Fluid Interfaces and Confined Fluids: Non-Local Versus Local Density Functionals. *Mol. Phys.* **1987**, *60*, 573–595.

(22) Lastoskie, C.; Gubbins, K. E.; Quirke, N. Pore Size Distribution Analysis of Microporous Carbons: a Density Functional Theory Approach. *J. Phys. Chem.* **1993**, *97*, 4786–4796.

(23) Horváth, G.; Kawazoe, K. Method for the Calculation of Effective Pore Size Distribution in Molecular Sieve Carbon. *J. Chem. Eng. Jpn.* **1983**, *16*, 470–475.

(24) Everett, D. H.; Powl, J. C. Adsorption in Slit-like and Cylindrical Micropores in the Henry's Law Region. *J. Chem. Soc., Faraday Trans. 1*, **1976**, *72*, 619–636.

(25) Schwalbe, S.; Trepte, K.; Seifert, G.; Kortus, J. Screening for High-Spin Metal Organic Frameworks (MOFs): Density Functional Theory Study on DUT-8($M_1$,$M_2$) (with $M_i$ = V,...,Cu). *Phys. Chem. Chem. Phys*. **2016**, *18*, 8075–8080.

(26) Dangi, G. P.; Pillai, R. S.; Somani, R. S.; Bajaj, H. C.; Jasra, R. V. A Density Functional Theory Study on the Interaction of Hydrogen Molecule with MOF-177. *Mol. Simul.* **2010**, *36*, 373–381.

(27) Wilbraham, L.; Coudert, F. X.; Ciofini, I. Modelling Photophysical Properties of Metal-Organic Frameworks: A Density Functional Theory Based Approach. *Phys. Chem. Chem. Phys*. **2016**, *18*, 25176–25182.

(28) Shao, Y.; Gan, Z.; Epifanovsky, E.; Gilbert, A. T.; Wormit, M.; Kussmann, J.; Lange, A. W.; Behn, A.; Deng, J.; Feng, X.; Ghosh, D.; Goldey, M.; Horn, P. R.; Jacobson, L. D.; Kaliman, I.; Khaliullin, R. Z.; Ku_s, T.; Landau, A.; Liu, J.; Proynov, E. I.; Rhee, Y. M.; Richard, R. M.; Rohrdanz, M. A.; Steele, R. P.; Sundstrom, E. J.; Woodcock, H. L.; Zimmerman, P. M.; Zuev, D.; Albrecht, B.; Alguire, E.; Austin, B.; Beran, G. J.; Bernard, Y. A.; Berquist, E.; Brandhorst, K.; Bravaya, K. B.; Brown, S. T.; Casanova, D.; Chang, C. M.; Chen, Y.; Chien, S. H.; Closser, K. D.; Crittenden, D. L.; Diedenhofen, M.; Distasio, R. A.; Do, H.; Dutoi, A. D.; Edgar, R. G.; Fatehi, S.; Fusti-Molnar, L.; Ghysels, A.; Golubeva-Zadorozhnaya, A.; Gomes, J.; Hanson-Heine, M. W.; Harbach, P. H.; Hauser, A. W.; Hohenstein, E. G.; Holden, Z. C.; Jagau, T. C.; Ji, H.; Kaduk, B.; Khistyaev, K.; Kim, J.; Kim, J.; King, R. A.; Klunzinger, P.; Kosenkov, D.; Kowalczyk, T.; Krauter, C. M.; Lao, K. U.; Laurent, A. D.; Lawler, K. V.; Levchenko, S. V.; Lin, C. Y.; Liu, F.; Livshits, E.; Lochan, R. C.; Luenser, A.; Manohar, P.; Manzer, S. F.; Mao, S. P.; Mardirossian, N.; Marenich, A. V.; Maurer, S. A.; Mayhall, N. J.; Neuscamman, E.; Oana, C. M.; Olivares-Amaya, R.; Oneill, D. P.; Parkhill, J. A.; Perrine, T. M.; Peverati, R.; Prociuk, A.; Rehn, D. R.; Rosta, E.; Russ, N. J.; Sharada, S. M.; Sharma, S.; Small, D. W.; Sodt, A.; Stein, T.; St□uck, D.; Su, Y. C.; Thom, A. J.; Tsuchimochi, T.; Vanovschi, V.; Vogt, L.; Vydrov, O.; Wang, T.; Watson, M. A.; Wenzel, J.; White, A.; Williams, C. F.; Yang, J.; Yeganeh, S.; Yost, S. R.; You, Z. Q.;

Zhang, I. Y.; Zhang, X.; Zhao, Y.; Brooks, B. R.; Chan, G. K.; Chipman, D. M.; Cramer, C. J.; Goddard, W. A.; Gordon, M. S.; Hehre, W. J.; Klamt, A.; Schaefer, H. F.; Schmidt, M. W.; Sherrill, C. D.; Truhlar, D. G.; Warshel, A.; Xu, X.; Aspuru-Guzik, A.; Baer, R.; Bell, A. T.; Besley, N. A.; Chai, J. D.; Dreuw, A.; Dunietz, B. D.; Furlani, T. R.; Gwaltney, S. R.; Hsu, C. P.; Jung, Y.; Kong, J.; Lambrecht, D. S.; Liang, W.; Ochsenfeld, C.; Rassolov, V. A.; Slipchenko, L. V.; Subotnik, J. E.; Van Voorhis, T.; Herbert, J. M.; Krylov, A. I.; Gill, P. M. W.; Head-Gordon, M. Advances in Molecular Quantum Chemistry Contained in the Q-Chem 4 Program Package. *Mol. Phys*. **2015**, *113*, 184–215.

**For Table of Contents Use Only**

Experimental, Structural, and Computational Investigations of Mixed Metal-Organic Frameworks from Regioisomeric Ligands for Porosity Controls

Dopil Kim,[†,#] Hyeonbin Ha,[†,#] Youngik Kim,[†] Younghu Son,[‡] Jiyoon Choi,[§,∥] Myung Hwan Park,[¶] Youngjo Kim,[†] Minyoung Yoon,*[,‡] Hyungjun Kim,*[,§,∥] Dongwook Kim,*[,Δ] and Min Kim*[,†]

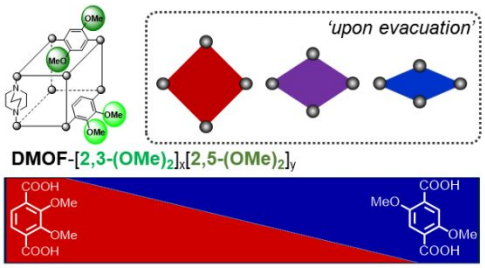


**Synopsis:** Porosity controls of pillared metal-organic frameworks (MOFs) have been achieved using regioisomeric ligand mixtures. The quantity of $N_2$ absorbed was tuned between 20~300 $cm^3/g$ upon ligand-mixing ratio of dimethoxy-functionalized regioisomers. Collaboration between synthesis, detail structural analysis, and computational approaches revealed that the significant differences of the coordination environments between regioisomeric MOFs.